Journal of Materials Chemistry A

Accepted Manuscript

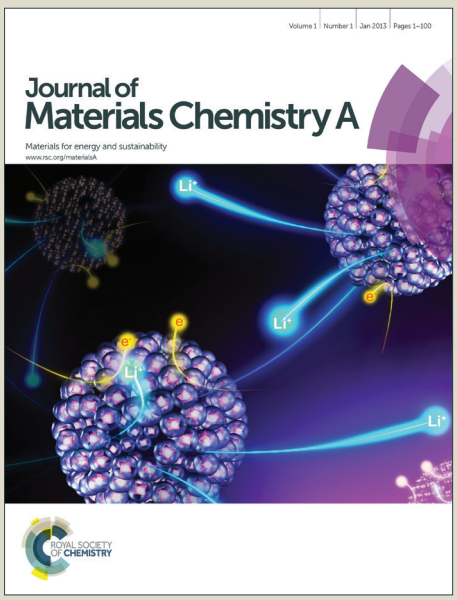

ROYAL SOCIETY OF CHEMISTRY

www.rsc.org/materialsA

Table of content

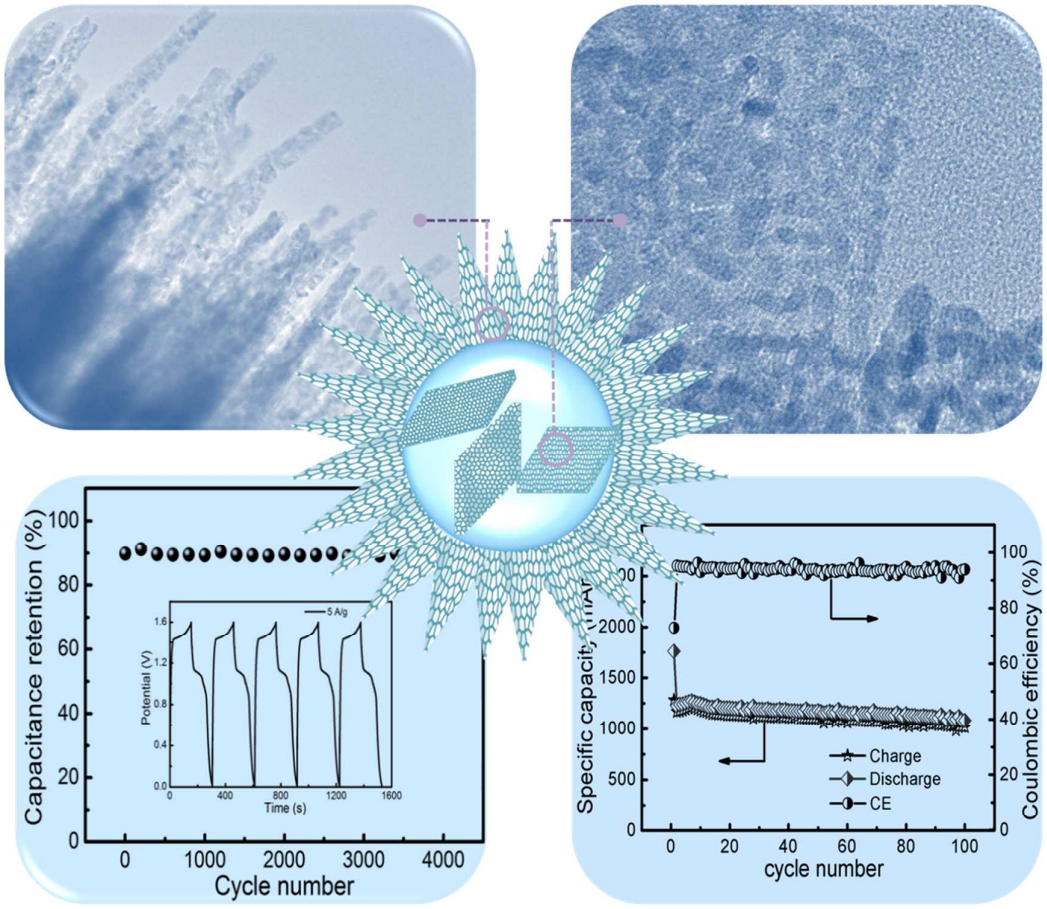

Herein, the unique dandelion-like $NiCo_2O_4$microspheres@nanomeshes have been successfully fabricated through a simple template-free solvothermal method, which display superior electrochemical performances as electrode materials of supercapacitor and lithium-ion battery.

Self-assembled novel dandelion-like NiCo2O4 microspheres@nanomeshes with superior electrochemical performance for supercapacitors and lithium-ion batteries

Li Liu, Huijuan Zhang, Jiao Yang, Yanping Mu, Yu Wang*

The State Key Laboratory of Mechanical Transmissions and the School of Chemistry and Chemical Engineering, Chongqing University, 174 Shazheng Street, Shapingba District, Chongqing City, P.R. China, 400044

E-mail: *wangy@cqu.edu.cn; prospectwy@gmail.com*

Supporting information for this article is available.

Keywords: $NiCo_2O_4$, Microsphere, Nanomesh, Supercapacitor, Lithium-ion battery

Abstract

Binary metal oxides have been regarded as potential electrode materials for supercapacitor and lithium-ion battery, which can ameliorate and compensate the deficiency of electrochemical performance of the single metal oxides, such as reversible capacitance/capacity, structural stability and electronic conductivity. In this work, we report a facile solvothermal method to synthesize the hierarchical dandelion-like $NiCo_2O_4$ microspheres @nanomeshes (NCO-M@N) with high surface area (105.2 m^2 g^{-1}), which exhibit superior pseudocapacitive performance with high specific capacitance (2184 F g^{-1}), remarkable rate capability and excellent cycling performance (94.2% retention after 4000 cycles), meanwhile, display excellent energy storage properties for lithium-ion battery, such as admirable rate performance(785mAh g^{-1} at a current density of 2000 mA g^{-1}) and outstanding capacity retention of 88 % after 100 cycles. Most importantly, when the NCO-M@N//AC asymmetric supercapacitor is prepared, it exhibits the highest energy density (45.3 Wh kg^{-1}) at a power density of 533.3 W $kg^{-1}$and good cycling stability (89% of the initial capacitance retention at 5 Ag^{-1} over 4000 cycles), indicating its potential applications for next-generation high power supercapacitor and lithium-ion battery. The strategy is simple but very effective, thus it can be extended to other high-capacity metal oxide materials.

Introduction

With the fast-growing energy requirements in electrical energy storage for electric vehicles and mobile electronics, the development of clean, sustainable and renewable energy storage systems has attracted extensive research interest worldwide.[1, 2] Among various energy storage systems, such as capacitors[3, 4], lithium-ion batteries (LIBs)[5], fuel cells[6, 7] and so on, supercapacitors (SCs)[2, 8, 9] and LIBs [10, 11] have been suggested to be the most promising energy storage devices for their high power density, long cycle lifetime and fast charging-discharging rates. Generally, supercapacitors can be divided into two categories based on the different charge storage mechanisms, traditional electrochemical double layer capacitors and pseudocapacitors.[12] Thereinto, pseudocapacitor owns a higher specific capacitance, taking advantage of reversible Faradaic reactions at the electrode surface. Thus, it could have potential applications in portable electronics and a number of microdevices.[13, 14] Similarly, lithium-ion battery has also progressively attracted extensive interests within the industrial and scientific communities. And it is now the dominative power source for portable electronics and electric/hybrid electric cars.[10, 11, 15] However, to meet the increasing energy demands, the energy density and power density of both SCs and LIBs should be increased without sacrificing the cycle life.[16, 17] As is well known, the electrochemical performance of SCs and LIBs is largely determined by the properties of electrode materials.[18]

Therefore, it is imperative to develop novel electrode materials/structures with superior electrochemical performance but a low cost for the development of SCs and LIBs. Several promising materials, including nickel oxide, cobalt oxide and manganese oxide, have been intensively studied as advanced electrode materials for SCs and LIBs.[19-21] However, as the previously reported, metal oxides commonly suffer from poor stability, low conductivity and large volume changes during the charge/discharge process, which limits their commercial attractiveness.[16, 22]

Binary metal oxides, such as $NiCo_2O_4$,[23, 24] $ZnCo_2O_4$,[25, 26] $CuCo_2O_4$[27, 28] and $ZnMn_2O_4$[29, 30] have recently been investigated as advanced electrode materials for SCs and LIBs. Among the various binary metal oxides mentioned above, $NiCo_2O_4$ is considered as the most promising electrode material due to its high theoretical capacity (890 mAh g^{-1}), low diffusion resistance to ions and easily penetration of electrolyte.[31, 32] Particularly, $NiCo_2O_4$ possesses higher electric conductivity, at least two orders of magnitude higher than nickel oxide and cobalt oxide.[33, 34] The higher electronic conductivity is benefit to the rapid transfer of electrons in an electrode. Obviously, these prominent features are in favor of the development of high-performance electrode materials. To date, many methods, including hydrothermal,[35] sol-gel,[36] electrodeposition,[37] microwave[38] and so on, have been used to prepare $NiCo_2O_4$ with different morphology, for instance, nanoneedle,[39] nanosheets,[40] nanospheres,[41] *etc*. Lou and co-works have synthesized $NiCo_2O_4$ nanosheets/nanowires on conductive substrates for achieving excellent cycling performance and rate capability,[42] and meanwhile they have also prepared the ultrathin mesoporous $NiCo_2O_4$ nanosheet on nickel foam showing a specific capacitance of 1450 F g^{-1} at 20 A g^{-1}.[43] Qian and co-works have reported monodisperse $NiCo_2O_4$ mesoporous microspheres by a solvothermal method with subsequent annealing of the precursor, which display good battery performance.[44] Additionally, Dan and co-works have produced the hollow urchin-like $NiCo_2O_4$ microspheres, which reveal a relatively high specific capacitance (95 F g^{-1} at a current density of 1 Ag^{-1}) and remarkable energy density (~36 Wh kg^{-1} at the power density of 852 W kg^{-1}).[45] Although the hollow $NiCo_2O_4$ microsphere achieved great progress in terms of electrochemical performance, the hollow structures fail to take advantage of the internal space, leading to the low tap density. However, this problem could be solved by synthesizing a novel and hierarchical micro/nanostructured $NiCo_2O_4$ microspheres with some 2D nanomeshes on the inside, which special structure can make the best use of the internal space. Despite the fact that great effort has been made, it is still a big challenge to produce hierarchical micro/nanostructured $NiCo_2O_4$ microspheres with nanomeshes on the inside.

Herein, attracted by the outstanding electrochemical performance of $NiCo_2O_4$, we report a simple template-free solvothermal route, followed by the thermal post-treatment of precursor, to synthesize the hierarchical dandelion-like $NiCo_2O_4$ porous microspheres@nanomeshes (records as NCO-M@N), which numerous porous nanoneedles radially grow on the surface of the microsphere and some porous nanomeshes orderly grow on the inside. We observed an interesting structural evolution process from solid nanoneedle-assembled microspheres to hierarchical dandelion-like $NiCo_2O_4$ porous microspheres@nanomeshes. In this process, the weakly alkaline urea as a precipitant and the isopropyl alcohol as a structure modifier jointly play an important role in designing the novel morphology. The as-prepared hierarchical dandelion-like $NiCo_2O_4$ porous microspheres@nanomeshes acting as electrode materials for supercapacitors and lithium-ion batteries, respectively, exhibit the improved electrochemical performance. It is found that the as-synthesized sample has a relatively high surface area of 105.2 m^2 g^{-1} and a narrow pore size distribution of 8-15 nm (centered at 10.1 nm). Especially, to demonstrate the principle of boosting energy density, asymmetric supercapacitors (ASCs) are constructed by employing the as-synthesized sample for positive electrode and activated carbon (AC) for the negative electrode, and the ASCs device have extended the cell voltage to 1.6 V in 2 M KOH aqueous electrolyte, achieving remarkable energy density (45.3Wh kg^{-1}), high power density and cycling stability. So far, there is no report on synthesizing the novel hierarchical dandelion-like $NiCo_2O_4$ porous microspheres@nanomeshes on the inside, which is evaluated as the

electrode materials for SCs and LIBs. The effective strategy is versatile and could be extended to other high performance binary metal oxides with similar structure for next generation high energy storage systems.

Results and Discussions

The X-ray diffraction (XRD) patterns, Figure S1a (supporting information) and Figure 1a, reveal the overall crystal structure and phase purity of the as-prepared products. The Co-Ni bimetallic carbonate hydroxide salts ($NiCo_2(OH)_{3y}(CO_3)_{1.5(2-y)} \cdot n\ H_2O$) were formed at the molar ratio of Co/Ni at 2:1, as shown in Figure S1a, and then decomposed into the $NiCo_2O_4$ in the following annealing process. Figure 1a demonstrates that all diffraction peaks can be indexed to the cubic phase $NiCo_2O_4$, in good agreement with the reported values from the JCPDS card No. 20-0781. There are no other additional diffraction peaks in the pattern, indicating the high phase purity of $NiCo_2O_4$ formed. In addition, the strong intensity and narrow peak width suggest $NiCo_2O_4$ has high crystallinity. These above results definitely confirm that the adopted synthesis strategy successfully achieves pure $NiCo_2O_4$. Meanwhile, the chemical compositions of the products, as analyzed by EDS spectroscopy (Figure S1b), testify the atomic ratio of Ni:Co is approximately 1: 2, consistent with the stoichiometric ratio of $NiCo_2O_4$. XPS measurements are also implemented to discern the chemical composition and elemental chemical state on the surface of hierarchical dandelion-like NCO-M@N and the results are shown in Figure 1b-1d. By using a Gassian fitting method, the Co 2p emission spectrum was well fitted, displaying two spin-orbit doublets characteristic of Co^{2+} and Co^{3+}.[46] The fitting peaks at binding energies of 779.3 eV and 794.4 eV are ascribed to Co^{3+}, as shown in Figure 1b, while the peaks at 781.0 eV and 795.7 eV are indexed to Co^{2+}.[47] In the Ni 2p spectrum (Figure 1c), two kinds of Ni species (Ni^{2+} and Ni^{3+}) were also detected. The Ni 2p spectrum consists of two spin-orbit doublets and two shakeup satellites (denoted as sat.). The fitting peaks at 854.0 eV and 871.6 eV are attributed to Ni^{2+}, while the fitting peaks at 855.8 eV and 873.8 eV are indexed to Ni^{3+}.[48] Meanwhile, the satellite peaks at 861.0 eV and 879.4 eV are two shake-up type peaks of Ni at the high binding energy side of the $Ni2p_{3/2}$ and $Ni2p_{1/2}$ edge, respectively.[49] Besides, Figure 1d displays the high resolution spectrum for O1s, which exhibits three oxygen species marked as O1, O2 and O3. According to previous reports, the fitting peak of O1 at a binding energy of 529.6 eV is a typical metal-oxygen bond.[47] And the fitting peak of O2 at 531.2 eV could be attributed to a high number of deflect sites with low oxygen coordination in the material.[50] The fitting peak of O3 at 532.4 eV can be ascribed to the multiplicity of physic- and chemisorbed water at and within the surface.[47] Thus, these XPS results prove that the surface of the as-prepared hierarchical dandelion-like NCO-M@N has a mixed composition containing Co^{2+},Co^{3+},Ni^{2+} and Ni^{3+}, which is in agreement with previous reports[48, 51]. The solid redox couple of Ni^{2+}/Ni^{3+} and Co^{2+}/Co^{3+} can offer enough active sites and rich redox reactions, which may be one of the important factors contributing to the high electrochemical performance.

The morphological and structural features of precursor and NCO-M@N are examined by low and high resolution scanning electron microscope (SEM). Figure S2 (supporting information) exhibits the SEM images of Co-Ni bimetallic carbonate hydroxide salts precursors. As shown in Figure S2, a large scale of microspheres with a diameter of about 2-5 μm have been obtained, demonstrating that the strategy would be applied in large-scale commercial production. Figure 2a displays the individual microsphere of the bimetallic carbonate hydroxide salts precursors, from which the dandelion-like hierarchical structure with numerous nanoneedles radially grown on the surface can be clearly detected. Figure 2b shows the low-magnification SEM images of as-synthesized dandelion-like NCO-M@N. Remarkably, the hierarchical micro/nanostructure was maintained even after thermal treatment of the precursors, as shown in Figure 2b. There is no obvious change in morphology, suggesting excellent structural stability. Furthermore, the close observation of the inset in Figure 2b shows the nanoneedles, the building blocks of the NCO-M@N, become much rougher in contrast to that of precursors after calcination. Moreover, the nanoneedles exhibit the average diameter of 10-20 nm and length of up to 1-2 μm. To further discern the unique structures, the cracked microsphere of NCO-M@N is shown in Figure 2c. It is obvious that

these microspheres possess the novel structure of hollow cavity, which is surrounded by the building blocks of nanoneedles, and some 2D sheet-like nanomeshes inlay in the hollow cavity. Undoubtedly, the unique 3D structure can compensate the defect of hollow structural materials by making use of the internal space, enhancing the energy density. Moreover, according to Figure 2c, the thickness of the walls around the hollow cavity is about 100 nm, which may be beneficial to form ion-buffering reservoirs at the center and shorten ion transport pathway. Figure 2d is the enlarged SEM image of NCO-M@N, located in the white rectangle box of Figure 2c, which reveals the detailed structure feature of the nanomeshes on the inside. From Figure 2d, it can be seen that the nanomeshes exhibit a 2D sheet-like shape, with lengths of 1-2μm, widths of 500-600 nm as well as thickness of 10-15 nm, and consist of numerous mesoporous structure.

We further fell back on transmission electron microscopy (TEM), high-resolution transmission electron microscope (HRTEM) and selected-area electron diffraction (SAED) to identify the detailed morphological and crystallographic properties of the as-fabricated NCO-M@N. Typical TEM image in Figure 3a displays each microsphere is composed of numerous primary nanoneedles, and the diameter of the microsphere is centered at around 2-5 μm, in well accordance with Figure S2. The TEM image (Figure 3b), taken from the marked area of Figure 3a, reveals that nanoneedles on the edges of NCO-M@N consist of numerous small nanoparticles and a large portion of mesoporous structure, which is ascribed to the fact that the H_2O, CO_2 and NH_3 gases are released and lost during the intermediates' decomposition/oxidation through thermal annealing. Figure 3c presents the TEM image of internal $NiCo_2O_4$ nanomesh, obtained from the cracked microsphere structure broken by the powerful ultrasonic. From Figure 3c, a distinct light-dark contrast is obviously observed in the $NiCo_2O_4$ nanomesh, revealing that the $NiCo_2O_4$ nanomesh is decorated with porous structure on their surface. The porous structure infers that the materials could be endowed with high specific surface area. For better insight into the surface area and pore size distribution of NCO-M@N, BET method was used for further measurement. The nitrogen absorption-desorption isotherm and the pore size distribution profiles are exhibited in Figure S3 and the inset image, respectively. The adsorption and desorption isothermal of NCO-M@N with an obvious hysteresis loop in the range of *ca.* 0.5-1.0 p/p_0, which infers the existence of a large number of mesoporous structures.[52] According to Figure S3, the surface area of NCO-M@N is 105.21 $m^2 g^{-1}$ and a narrow pore size distribution (8-15 nm) is mainly centered at 10.1 nm. The HRTEM image (Figure 3d) of an individual nanoneedle with randomly orientated lattice phase infers the polycrystalline characteristic of the as-harvested product. Furthermore, as shown in Figure 3d, the *d*-spacings of 0.25, 0.28 and 0.47 nm index to the distance of the (311), (220) and (111) planes of the $NiCo_2O_4$ crystal, respectively. The corresponding typical selected-are electron diffraction (SAED) image, the inset of Figure 3d, displays the well-defined rings, further confirming the polycrystalline nature of samples. These results are identical with the aforementioned results from XRD and HRTEM. What's more, the elemental mapping was performed to demonstrate the chemical components and the spatial distribution of the corresponding elements in the NCO-M@N, as shown in Figure 4. The mapping results unambiguously certify that Co, Ni and O atoms uniformly distributed within the whole NCO-M@N.

To better explain the reaction mechanisms responsible for the formation of the dandelion-like NCO-M@N, time-dependent experiments were carried out. On the basis of the precursor morphology as a function of reaction time (Figure 5) and the SEM image results from Figure 2, a possible formation process is put forward in Scheme 1. Herein, metal cations, such as Co^{2+} and Ni^{2+}, react with CO_3^{2-} and OH^- anions, which are released from hydrolysis of urea, contributing to the formation of precursors. The relevant reactions can be expressed as follows:

$CO(NH_2)_2 + H_2O \rightarrow CO_2 + 2NH_3$……. (1)

$CO_2 + H_2O \rightarrow H_2CO_3 \rightarrow CO_3^{2-} + 2H^+$…….. (2)

$NH_3 + H_2O \rightarrow NH_3 \cdot H_2O \rightarrow NH_4^+ + OH^-$……..… (3)

$(Co^{2+} + Ni^{2+}) + xOH^- + 0.5(2-X)CO_3^{2-} + nH_2O \rightarrow (Co, Ni)(OH)_x(CO_3)_{0.5(2-x)} \cdot nH_2O$……(4)

In the initial reaction stage, a large number of initial crystal nuclei start to come into being. Owing to the high surface energy, the freshly formed crystal nanonuclei are thermodynamically unstable, thus they tend to gather together to minimize the interfacial energy, causing the supersaturated nuclei aggregate together.[53] Afterwards, in the following stage, the aggregated nuclei serve as nucleation centers to allow the subsequent adsorption of newly formed nuclei and the growth of primary crystals. For the reason that the electronic structure of Co^{2+} (prefer octahedral coordination) and Ni^{2+} (prefer square-planar coordination) is different, the growth along the c-axis is the fastest leading to the formation of 1D nanoneedles.[54] Then, these nanoneedles self-assembled into solid microspheres. As reaction time prolongs, they gradually blossom into robust and well-rounded dandelion-like microspheres. After that, the nanoneedles-assembled microspheres undergo the Ostwald ripening process to form the void space in the internal of the microsphere. Following, due to the existence of some space in the internal of microsphere, the internal nuclei recrystallize into 2D nanosheet to make best use of the limited space. It is worth noting that the isopropyl alcohol molecules, as surfactant, play a role in dispersing the individual dandelion-like precursors. In order to verify the reaction mechanisms, the corresponding SEM images of the evolution process are presented in Figure S4 and Figure 5. Figure S4 displays the morphology of precursor obtained after reaction for 30 min, from which a mass of initial crystal nuclei begin growing and aggregating together to form spheroidal morphology. Then, as shown in Figure 5a, the nanoneedle-assembled microspheres are obtained after reaction duration for 1 h, and the nanoneedles become denser after solvothermal treatment for 2 h (Figure 5b). When the reaction continues 4 h, the internal nanonuclei begin to grow as shown in Figure 5c. When the reaction time is prolonged to 6 h, 7 h and 8 h, as displayed in Figure 5d, 5e and 5f, respectively, the internal nanomeshes are undergoing growth and final formation, accompanied with Ostwald ripening process to form the void space in the internal of the microsphere. Continuing to prolong the reaction time for 9 h, the building blocks of nanoneedles start to become bulky (Figure 5g). Finally, the microcube-like precursors are obtained when the reaction duration was extended to 10 h. Obviously, when the reaction continues 8h, the hybrid structure, which numerous nanoneedles radially grow on the surface to form the dandelion-like microsphere and the 2D nanomeshes orderly develop on the inside of the hollow cavity, is completely formed. In this case, the novel hybrid structure is beneficial to relieve the strain induced by the volume expansion associated with the redox reactions and Li^+ intercalation/deintercalation process. Undoubtedly, the optimized reaction time for the NCO-M@N is 8 hours. These results reveal that the growth of the nanoneedles structure on the exterior surface of the microsphere is accompanied by the recrystallization to form nanomeshes, taken place at the internal of the microspheres. The above experimental observations demonstrate that a plausible formation mechanism of dandelion-like microspheres@nanomeshes precursors is proposed.

In order to clearly illustrate the morphology superiority, the electrochemical properties of the NCO-M@N electrodes are further evaluated and shown in Figure 6. The cyclic voltammogram (CV) tests of the as-prepared NCO-M@N were firstly carried out in a three-electrode configuration with a Pt plate counter electrode and a SCE reference electrode in 2 M KOH aqueous electrolyte. Figure 6a denotes the CV curves of the NCO-M@N electrode at various scan rates of 10-50 mVs^{-1} in the potential range of 0-0.6 V. As expected, the CV curves of the NCO-M@N exhibit the strong peak and big area suggesting the high electrochemical reaction activity. Besides, a coupled pair of well-defined redox peaks is observed in anodic and cathodic sweeps in all CV curves, indicating that the measured capacitance is mainly based on the redox mechanism. And the redox peaks are mainly attributed to the following redox reaction:

$NiCo_2O_4 + OH^- + H_2O \rightarrow NiOOH + 2CoOOH + 2e^-$…….. (5)

$CoOOH + OH^- \rightarrow CoO_2 + H_2O + e^-$……... (6)

More interesting, only one cathodic peak is obviously detected, which could be ascribed to the similar redox potential of Co_3O_4 and NiO resulting in the appreciable broadening of some redox peaks.[55] Furthermore, the redox

peaks in these CV curves are maintained at different scan rates, revealing the superior kinetic reversibility. It should be noted that with increasing scan rate, the redox current increased. Moreover, the anodic and cathodic peak potentials shifted towards more anodic and cathodic directions, respectively, thus the capacitance inevitably decreased. In order to get more information about the performance of the NCO-M@N electrodes, galvanostatic charge-discharge measurements were further conducted in the voltage range between 0.01 and 0.5 V (*vs*. Ag/AgCl). As shown in Figure 6b, the NCO-M@N electrode demonstrates considerably long discharging time, implying the high specific capacitance values based on the computational formula of capacitance Ⅰ. On the side, the specific capacitance of the NCO-M@N electrodes can be calculated based on Figure 6b and typical data are presented in Figure 6c. Impressively, the NCO-M@N electrode delivers high specific capacitance of 2184, 2138, 1972, 1848 and 1728 F g^{-1} at current densities of 1, 2, 5, 10 and 20 A g^{-1}, respectively. To the best of our knowledge, the good electrochemical performances of the NCO-M@N electrode material are considerably better than previously reported values of hybrid nanostructures, for instance, hierarchical $NiCo_2O_4$ nanowires (760 F g^{-1}at the current density of 1 A g^{-1}), hierarchical $NiCo_2O_4$ nanosheets (778 F g^{-1} at 2 A g^{-1}) and single-crystal $NiCo_2O_4$ nanoneedle arrays (1118.6 F g^{-1} at the current density of about 6 A g^{-1}), as listed in Table S1. Besides, it is worth noting that the nickel foam has little capacitance contribution to the whole capacitance of the NCO-M@N electrode material, as shown in Figure S5, which the pure Ni foam possesses the specific capacitance of only 36.2 F g^{-1}. Thus, in this case, the contribution of nickel foam to the total specific capacitance of the NCO-M@N electrode material is about 1.6%.

A long-term cycle stability of the as-synthesized products as an electrode material was evaluated, because the cycling performance plays an important role in determining the supercapacitors for many practical applications. As shown in Figure 6d, the specific capacitance can still be retained at about 94.2% after 4000 cycles at a large current density of 5 A g^{-1}, indicating excellent cycling stability. The improved supercapacitive performances of the NCO-M@N electrodes are mainly attributed to their unique mesoporous microspheres@nanomeshes structure, which provides more active sites for efficient electrolyte ion transportation not only at the active materials surface but also throughout the bulk.

To further evaluate the NCO-M@N electrode for practical application, an asymmetric supercapacitor (denoted as NCO-M@N//AC-ASC) was fabricated by utilizing the NCO-M@N sample and activated carbon (AC) on nickel foam as the positive and negative electrodes, respectively. As is well known, theapplied voltage of symmetric supercapacitor can split equally between the two electrodes due to using the same material and the same mass in each electrode. However, in ASCs, the voltage split depends on the capacitance of each electrode active material and ASC can avoid the aqueous electrolyte decomposition at 1 V which occurs in the symmetric supercapacitors.[56] Hence, ASCs can take advantage of different potential windows of the two electrodes to increase the maximum operating voltage of the device in the aqueous electrolyte (up to 1.6 V). Figure S6 displays the comparative CV curves of the NCO-M@N and AC electrodes at a scan rate of 10 mV s^{-1}, suggesting the ASCs can deliver a device with 1.6 V operation voltage, which is higher than that of conventional AC-based symmetric supercapacitors (0.8-1.0 V). Accordingly, in the subsequent electrochemical performance assessment of the NCO-M@N//AC-ASC, the potential window of 0.01-1.6 V is employed. Figure 7a shows the CV curves of the asymmetric supercapacitor at scan rates of 10-50 mV s^{-1}, which demonstrate obvious oxidation and reduction peaks, revealing the typical pseudocapacitive property. Figure 7b displays the Galvanostatic charge-discharge (GCD) curves of the ASCs at different current density and its corresponding specific capacitance is shown in Figure 7c. The mass specific capacitance of NCO-M@N//AC-ASC can achieve the maximum specific capacitance of 127.5 F g^{-1} at 1 A g^{-1}, which is substantially higher than the values reported previously (see Table S2). Besides, power density and energy density are the two key parameters to evaluate the performance of supercapacitors. Based on the GCD curves of the ASC, the energy density (*E*) and power density (*P*) could be calculated from the eq Ⅱand Ⅲ. The ASC can

deliver maximum energy density of 45.3 Wh kg^{-1} at a power density of 533.3 W kg^{-1}. In addition, the cycling stability of the NCO-M@N//AC-ASC was evaluated by a repetitive charge-discharge test, as shown in Figure 7d and the inset image. As expected, the ASCs exhibit outstanding electrochemical stability, and maintain as much as 89% of its original capacitance value at a constant current density of 5 Ag^{-1}. The above results demonstrate the outstanding performance of these asymmetric supercapacitors and the electroactive material in practical applications.

As the unique porous structure combined with high surface area, the as-synthesized NCO-M@N may display potential applications in a variety of field. To evaluate whether the NCO-M@N would be applicable in lithium-ion batteries, the as-prepared product was used as anode materials in tests. Figure 8a presents the first three cyclic voltammetry (CV) curves of the NCO-M@N electrode at a scan rate of 0.1 mV s^{-1} in the range of 0.01-3.0 V. An irreversible reduction peak is observed at 0.73 V in the first cycle, corresponding to the initial reduction of $NiCo_2O_4$ to metallic cobalt and nickel, and the electrochemical formation of amorphous Li_2O. However, the broad peak at about 0.42 V corresponds to the formation of a solid electrolyte interface (SEI) layer. During the following anodic scan in the first cycle, the oxidation peak is located at 2.16 V, which are ascribed to the oxidation reaction and formation of Ni oxides and Co oxides. Then, in the subsequent cycles, the main cathodic peak is shifted to a higher potential at about 0.91 V, meanwhile the anodic peak position is located at 2.1 V, attributing to the reduction and oxidation of the nickel oxides and cobalt oxides.[57] This obvious shift might be correlated with some activation process resulted from Li^+ insertion in the first cycle, as reported in previous literature[58, 59]. This result suggests that the reduction becomes much easier in the subsequent cycles after the activation in the first cycle. Moreover, except the first cycle, the CV curves of the following cycles tend to overlap, indicating the high reversibility of lithium storage. On the basis of the CV measurements and the storage mechanisms of $NiCo_2O_4$, the whole electrochemical reaction is believed to be as follows:

$NiCo_2O_4 + 8Li^+ + 8e^- \rightarrow Ni + 2Co + 4Li_2O$ ..... (7)

$Ni + Li_2O \leftrightarrow NiO + 2Li^+ + 2e^-$ ..... (8)

$Co + Li_2O \leftrightarrow CoO + 2Li^+ + 2e^-$ ..... (9)

$CoO + 1/3\ Li_2O \leftrightarrow 1/3Co_3O_4 + 2/3Li^+ + 2/3e^-$ ..... (10)

Representative charge-discharge voltage profiles for the 1st, 2nd, 50th and 100th cycles of NCO-M@N electrode at a current density of 200 mA g^{-1}over the range of 0.01- 3.00 V *vs.* Li^+/Li at room temperature are displayed in Figure 8b. As shown in Figure 8b, there is a wide and steady discharging plateau at 1.0 V (*vs.* Li^+/Li) in the first cycle. The initial discharge and charge capacities are 1760 and 1284 mAh g^{-1} with the initial Coulombic efficiency of 73%, respectively. The formation of a solid electrolyte interphase (SEI) layer on the surface of active materials and the inactivation of some inserted Li-ion, which are common to most anode materials[60], may contribute to the initial extra capacity at the first discharge. The potential plateaus in the subsequent discharge curves shift upward to the higher voltage with a more sloping profile accompanied by a capacity loss, which could result from the irreversible reaction of $NiCo_2O_4$ and Li^+ as in eq (7).[61] Additionally, the consequent charge curves show a steady potential increase, meaning the increase of the overpotential, which could be ascribed to the polarization related to the ion transfer during the charge-discharge process. Furthermore, the discharge capacities at the 2nd, 50th and 100th cycles are approximately 1235.4, 1176.1, and 1086.6 mAh g^{-1}, respectively, suggesting outstanding capacity retention of NCO-M@N electrode. Figure 8c displays the Coulombic efficiency (CE), reversible capacity and cycling performance of the NCO-M@N electrode at a current density of 200 mA g^{-1}.The second discharge and charge capacities are 1235.4 and 1166 mAh g^{-1}, respectively. It is interesting to note that a trend of the slightly increased capacities before 10 cycles is detected, resulting from the slow kinetic activation process of the electrode. Afterwards, the reversible capacities decrease at a slow rate and finally maintain at about 1086 mAh g^{-1} after 100 cycles, with a high Coulombic efficiency of around 94%. Besides, the discharge capacity after 100 cycles is almost

88% of the second reversible capacity, illustrating the structural stability of the NCO-M@N through a long cycling process. In surprise, the Coulombic efficiencies of the first several cycles are relatively lower than those of the subsequent cycles, for the reason that the active materials do not completely contact with the electrolyte in the first several cycles. As the redox reaction proceeds, the phenomenon gradually disappears, which are well-documented in previous reports[62]. The rate performances were also evaluated to investigate the high power property of NCO-M@N electrode at various current densities (200-2000 mA g^{-1}) and the results are presented in Figure 8d. When the NCO-M@N electrode is cycled at 200, 500, 1000 and 2000 mA g^{-1} for 10 cycles, the corresponding average specific capacities of 1231, 1115, 964 and 785 mAh g^{-1}, respectively, are obtained at each of these current densities. Upon changing the current density back to 200 mA g^{-1}, an average discharge capacity as high as 1194 mAh g^{-1} could be recovered, verifying the excellent rate performance of NCO-M@N for high power lithium-ion batteries.

To further understand the superior electrochemical performance of NCO-M@N as anode material, the Nyquistpolts of $NiCo_2O_4$/Li cells were also employed to investigate the charge-transfer resistance before and after 100 cycles. Both the impedance spectra display a similar form with a semicircle in the high-frequency region and present a linear region over the low-frequency range, as shown in Figure S7. The Nyquist plots can be well fitted by employing an equivalent circuit (inset of Figure S7), where the Warburg impedance (Zw) corresponds to the linear region, which represents the electrolyte diffusion to the electrode surface; the solution resistance (Rs) corresponds to the intersection at the real part (Z'), consisting of the intrinsic resistance of the electroactive materials and electrolyte as well as the interface contact resistance; the charge transfer impedance (Rct) corresponds to the high frequency semicircle; CPE is a constant phase element accounting for a double-layer capacitor, and Cp is a pseudocapacitive element. From Figure S7, We can see that before and after tests, the bulk solution resistances Rs do not change much, while the slightly increase of charge transfer resistance (Rct) after cycling tests is observed, which is responsible for the capacity fading during the cycling process.

Multiple contributing factors can be considered for the high electrochemical performance of NCO-M@N. Firstly, the nanoscaled and interconnected $NiCo_2O_4$ nanoneedles offer large exposed surface with lots of electroactive sites for fast redox reactions and the interface for contacting between electrode and electrolyte, thus improving the high specific capacity and capacitance. Secondly, the existence of pores in the $NiCo_2O_4$ nanoneedles and nanomeshes is advantageous to ion and electron transport due to the shorter transport path, benefiting the high rate performance. Thirdly, the hybrid structure, which numerous nanoneedles radially grow on the surface to form the dandelion-like microsphere and the 2D nanomeshes orderly develop on the inside of the hollow cavity, is beneficial to relieve the strain induced by the volume expansion associated with the redox reactions and the Li^+ intercalation/ deintercalation process, thereby guaranteeing the long-term cycling stability. Besides, the unique structure could avoid "dead" volume caused by the tedious process of mixing active materials with polymer binder/conductive additives. Bearing those in mind, the structural features will undoubtedly bring about the superior electrochemical performance of the NCO-M@N electrode. However, the intrinsic high voltage plateau of such oxides may limit the practical application. To overcome the limitation and avoid the drawback, the nanostructured hybrid electrode materials doping with other metal cations are preferred and further investigation is under the way.

Conclusion

In summary, we have developed a simple template-free solvothermal method for the synthesis of hierarchical NCO-M@N, followed by annealing in air. The hybrid structural NCO-M@N consisting of numerous nanoneedles radially grown on the surface and some 2D nanomeshes orderly inlaid on the inside exhibits high specific surface area (105.2 m^2 g^{-1}) and a large number of pores with an average size of 10.1 nm. In view of the unique structural advantages, the NCO-M@N materials have been studied as advanced electrode materials for SCs and LIBs, respectively. When applied as an electrode material for supercapacitor, it achieves a specific capacitance of 2184 F

g^{-1} at a current density of 1 A g^{-1} with a stable operational voltage of 0.5 V. And the as-fabricated ASC device with an extended operating voltage window of 1.6 V achieved a specific capacitance of 127.5 F g^{-1} at current densities of 1 A g^{-1} and a maximum energy density of 45.3 Wh kg^{-1} at a power density of 533.3 W kg^{-1}. Besides, when used as an anode materials for LIBs, the as-synthesized NCO-M@N electrode displays a high specific capacity (1235.4 mAh g^{-1}), superior rate capacity (785 mAh g^{-1} at the current density of 2000 mA g^{-1}), excellent cyclability (Coulombic efficiency of 94%) and stability (capacity retention of 88% after 100 cycles). The improved electrochemical performance enables such hierarchical dandelion-like NCO-M@N to be a promising electrode material for next-generation supercapacitors and lithium-ion batteries.

Experimenntal section

Materials: all chemicals or materials were used as raw material without any further purification. Deionized water was used during all the experimental process. Isopropyl alcohol (Fisher Chemical, 99.97 %), anhydrous ethanol (Fisher Chemical, 99.99 %), cobalt nitrate hexahydrate ($Co(NO_3)_2 \cdot 6H_2O$, 99.9 %, Aldrich), nickel (Ⅱ) nitrate hexahydrate ($Ni(NO_3)_2 \cdot 6H_2O$, 99.9 %, Aldrich), potassium hydroxide (KOH, 90.0%, Aldrich), urea ($CO(NH_2)_2$, 99.9 %, Aldrich) and carbon black.

Materials Synthesis: The hierarchical dandelion-like $NiCo_2O_4$ porous microspheres@nanomeshes were prepared by a simple solvothermal method. In a typical synthesis, Isopropyl alcohol (15 mL), 1 M urea aqueous solution (12 mL), 1 M $Ni(NO_3)_2 \cdot 6H_2O$ aqueous solution (1 mL), 1 M $Co(NO_3)_2 \cdot 6H_2O$ aqueous solution (2 mL) and 3 mL deionized water were mixed step-by-step under strong stirring with intervals of 1-2 min. The resulting mixture was stirred for another 30 min and then the mixture changed into a light pink homogeneous solution. Once the mixture solution was transferred into a Teflon-lined stainless steel autocalve at a volume of 45 mL, a thermal treatment was performed for the Teflon liner in an electric oven at 120 ^oC for various reaction times. After the autoclave was cooled naturally to room temperature in air, the samples deposited at the bottom were collected and washed by centrifugation for at least three cycles by using deionized water and two cycles by using anhydrous ethanol. Finally, the as-prepared precursors were then dried in a vacuum oven at 60 ^oC overnight to remove the absorbed water for subsequent fabrication and characterization. Finally, the sample was placed into a quartz tube and annealed at 350 ^oC under air atmosphere for 2h. After calcinations, the pink purple precursors turned to black $NiCo_2O_4$ powder.

Characterization of the samples: field-emission SEM (JEOL JSM-7800F) coupled with an EDS analyzer (JEOL, JSM-7800F), TEM coupled with an EDX analyzer (Philips, Tecnai, F30, 300 kV), X-ray photoelectron spectrometery with a ESCALAB250 analyzer (XPS), powder X-ray diffraction (Bruker D8 Advance X-ray diffractometer with Cu K_α radiation (λ = 1.54184 Å)), Brunauer-Emmett-Teller surface area measurement (BET, Quantachrome Autosorb-6B surface area and Pore size analyzer) were used to characterize the obtained samples.

Electrochemical measurement: the working electrode was prepared with the active material, carbon black and polyvinyl difluoride (PVDF) binder in a weight of 80: 10: 10. A small amount of N-methylpyrrolidinone was added to the mixtures and then the slurries were cautiously coated on the nickel foam substrates (surface, 1 cm × 1 cm). After dried at 80 ^oC for 2 hours, the as-formed electrodes were then pressed at 10 Mpa and further dried at 80 ^oC for 1 day before use. The mass loading of active materials in a nickel foam electrode was about 1-1.5 mg cm^{-2}. Afterward, the obtained active material modified electrode was then used as a working electrode.

All electrochemical experiments of supercapacitor were carried out at room temperature using an electrochemical workstation (CHI660D, shanghai) in a three-electrode cell system. The prepared active material modified electrode as the working electrode was investigated with a slice of platinum foil (1 cm × 1 cm) as the auxiliary electrode and a standard calomel electrode (SCE) as the reference electrode. The measurements were carried out in two molar potassium hydroxide (KOH) aqueous electrolyte. Cyclic voltammetry (CV) tests were measured in a potential range between 0.0 and 0.6 V at various scan rates, and the charge-discharge processes were performed in the potential window from 0.01 to 0.5 V at different current densities. Specific capacitances were calculated using the below equation:

$C_m = I \times t / (m \times \triangle V)$ …… (Ⅰ)

Where I is the constant discharge current, t is the discharging time, V is the voltage drop upon discharging (excluding the *IR* drop), and m is the mass of the active material (includes the mass of active carbon).

In addition, the electrochemical properties of the asymmertric supercapacitor were further explored under a two-electrode cell using NCO-M@N active materials and carbon black as the positive and negative electrodes, respectively. The energy density (E) and power density (P) were also calculated as follows:

$E = 1/2\ C_m(\triangle V)^2$ ……(Ⅱ), $P = E/t$ ……(Ⅲ)

The electrochemical tests of lithium-ion battery were performed under ambient temperatures using two-electrode coin cells with lithium serving as both the counter electrode and the reference electrode. The active material slurries were spread onto Al foils as the working electrode and a polypropylene micro-porous film was employed as the separator. The electrolyte was a mixture of 1 M $LiPF_6$ in a mixture of DMC, EC and DEC (1: 1: 1, v/v/v). The assembly of the cells was carried out in an argon-filled glove box. Electrochemical impedance spectroscopy (EIS) was carried out using a CHI660D electrochemical workstation in the frequency range from 0.1 MHz to 0.01 Hz.

Acknowledgements

This work was financially supported by the Thousand Young Talents Program of the Chinese Central Government (Grant No. 0220002102003), National Natural Science Foundation of China (NSFC, Grant No. 21373280, 21403019), the Fundamental Research Funds for the Central Universities (0301005202017), Beijing National Laboratory for Molecular Sciences (BNLMS) and Hundred Talents Program at Chongqing University (Grant No. 0903005203205).

References and notes

1. J. M. Tarascon and M. Armand, *Nature*, 2001, **414**, 359-367.
2. J. R. Miller and P. Simon, *Science*, 2008, **321**, 651-652.
3. M. Beidaghi and Y. Gogotsi, *Energy Environ. Sci.*, 2014, **7**, 867-884.
4. V. Chabot, D. Higgins, A. Yu, X. Xiao, Z. Chen and J. Zhang, *Energy Environ. Sci.*, 2014, **7**, 1564-1596.
5. A. Kraytsberg and Y. Ein-Eli, *Adv. Energy Mater.*, 2012, **2**, 922-939.
6. H. Liu, C. Song, L. Zhang, J. Zhang, H. Wang and D. P. Wilkinson, *J. Power Sources*, 2006, **155**, 95-110.
7. S. Jiang, *J. Mater. Sci.*, 2008, **43**, 6799-6833.
8. C. Liu, F. Li, L.-P. Ma and H.-M. Cheng, *Adv. Mater.*, 2010, **22**, E28-E62.
9. H. Jiang, P. S. Lee and C. Li, *Energy Environ. Sci.*, 2013, **6**, 41-53.
10. P. G. Bruce, B. Scrosati and J.-M. Tarascon, *Angew. Chem. Int. Ed.*, 2008, **47**, 2930-2946.
11. A. S. Arico, P. Bruce, B. Scrosati, J.-M. Tarascon and W. van Schalkwijk, *Nat. Mater.*, 2005, **4**, 366-377.
12. L. Wang, Z. H. Dong, Z. G. Wang, F. X. Zhang and J. Jin, *Adv.Funct. Mater.*, 2013, **23**, 2758-2764.
13. M. F. El-Kady, V. Strong, S. Dubin and R. B. Kaner, *Science*, 2012, **335**, 1326-1330.
14. J.-H. Kim, K. Zhu, Y. Yan, C. L. Perkins and A. J. Frank, *Nano Lett.*, 2010, **10**, 4099-4104.
15. M. G. Kim and J. Cho, *Adv. Funct. Mater.*, 2009, **19**, 1497-1514.
16. J. Jiang, Y. Li, J. Liu, X. Huang, C. Yuan and X. W. Lou, *Adv. Mater.*, 2012, **24**, 5166-5180.
17. K. Xu, W. Li, Q. Liu, B. Li, X. Liu, L. An, Z. Chen, R. Zou and J. Hu, *J. Mater. Chem. A*, 2014, **2**, 4795-4802.
18. G. Wang, L. Zhang and J. Zhang, *Chem. Soc. Rev.*, 2012, **41**, 797-828.
19. Y. Wang, H. Xia, L. Lu and J. Lin, *Acs Nano*, 2010, **4**, 1425-1432.
20. Y. Wang, H. J. Zhang, L. Lu, L. P. Stubbs, C. C. Wong and J. Lin, *Acs Nano*, 2010, **4**, 4753-4761.
21. Y. Wang, H. J. Zhang, J. Wei, C. C. Wong, J. Lin and A. Borgna, *Energy & Environmental Science*, 2011, **4**, 1845-1854.
22. H. Zhang, X. Yu and P. V. Braun, *Nat. Nanotech.*, 2011, **6**, 277-281.
23. C. Yuan, H. B. Wu, Y. Xie and X. W. Lou, *Angew. Chem. Int. Ed.*, 2014, **53**, 1488-1504.
24. G. Zhang and X. W. Lou, *Advanced Materials*, 2013, **25**, 976-979.
25. Y. Sharma, N. Sharma, G. V. Subba Rao and B. V. R. Chowdari, *Adv. Funct. Mater.*, 2007, **17**, 2855-2861.
26. W. Luo, X. Hu, Y. Sun and Y. Huang, *J. Mater. Chem.*, 2012, **22**, 8916-8921.
27. Y. Sharma, N. Sharma, G. V. S. Rao and B. V. R. Chowdari, *J. Power Sources*, 2007, **173**, 495-501.
28. W. Kang, Y. Tang, W. Li, Z. Li, X. Yang, J. Xu and C.-S. Lee, *Nanoscale*, 2014, **6**, 6551-6556.
29. L. Zhou, H. B. Wu, T. Zhu and X. W. Lou, *J. Mater. Chem.*, 2012, **22**, 827-829.
30. G. Zhang, L. Yu, H. B. Wu, H. E. Hoster and X. W. Lou, *Adv. Mater.*, 2012, **24**, 4609-4613.
31. T.-Y. Wei, C.-H. Chen, H.-C. Chien, S.-Y. Lu and C.-C. Hu, *Adv. Mater.*, 2010, **22**, 347-351.
32. J. Xiao and S. Yang, *RSC Adv.*, 2011, **1**, 588-595.
33. Y. Li, P. Hasin and Y. Wu, *Adv. Mater.*, 2010, **22**, 1926-1929.
34. C. F. Windisch Jr, G. J. Exarhos, K. F. Ferris, M. H. Engelhard and D. C. Stewart, *Thin Solid Films*, 2001, **398–399**, 45-52.
35. N. Padmanathan and S. Selladurai, *RSC Adv.*, 2014, **4**, 8341-8349.
36. Y. Q. Wu, X. Y. Chen, P. T. Ji and Q. Q. Zhou, *Electrochim. Acta.*, 2011, **56**, 7517-7522.
37. L. Qian, L. Gu, L. Yang, H. Yuan and D. Xiao, *Nanoscale*, 2013, **5**, 7388-7396.
38. Y. Lei, J. Li, Y. Wang, L. Gu, Y. Chang, H. Yuan and D. Xiao, *ACS Appl. Mater. Interfaces*, 2014, **6**,

1773-1780.

39. G. Q. Zhang, H. B. Wu, H. E. Hoster, M. B. Chan-Park and X. W. Lou, *Energy Environ. Sci.*, 2012, **5**, 9453-9456.
40. W. Zhou, D. Kong, X. Jia, C. Ding, C. Cheng and G. Wen, *J. Mater. Chem. A*, 2014, **2**, 6310-6315.
41. Z.-Q. Shi, L.-X. Jiao, J. Sun, Z.-B. Chen, Y.-Z. Chen, X.-H. Zhu, J.-H. Zhou, X.-C. Zhou, X.-Z. Li and R. Li, *RSC Adv.*, 2014, **4**, 47-53.
42. G. Q. Zhang, H. B. Wu, H. E. Hoster, M. B. Chan-Park and X. W. Lou, *Energy Environ. Sci.*, 2012, **5**, 9453-9456.
43. C. Yuan, J. Li, L. Hou, X. Zhang, L. Shen and X. W. Lou, *Adv. Funct. Mater.*, 2012, **22**, 4592-4597.
44. J. Li, S. Xiong, Y. Liu, Z. Ju and Y. Qian, *ACS Appl. Mater. Interfaces*, 2013, **5**, 981-988.
45. Y. Lei, Y. Wang, W. Yang, H. Yuan and D. Xiao, *RSC Adv.*, 2015, **5**, 7575-7583.
46. Y. E. Roginskaya, O. V. Morozova, E. N. Lubnin, Y. E. Ulitina, G. V. Lopukhova and S. Trasatti, *Langmuir*, 1997, **13**, 4621-4627.
47. J. F. Marco, J. R. Gancedo, M. Gracia, J. L. Gautier, E. Ríos and F. J. Berry, *J. Solid State Chem.*, 2000, **153**, 74-81.
48. J. G. Kim, D. L. Pugmire, D. Battaglia and M. A. Langell, *Appl. Surf. Sci.*, 2000, **165**, 70-84.
49. J. Xiao and S. Yang, *J. Mater. Chem.*, 2012, **22**, 12253-12262.
50. V. M. Jiménez, A. Fernández, J. P. Espinós and A. R. González-Elipe, *J. Electron Spectrosc.Relat. Phenom.*, 1995, **71**, 61-71.
51. C. Yuan, J. Li, L. Hou, L. Yang, L. Shen and X. Zhang, *J. Mater. Chem.*, 2012, **22**, 16084-16090.
52. C. Yu, L. Zhang, J. Shi, J. Zhao, J. Gao and D. Yan, *Adv. Funct. Mater.*, 2008, **18**, 1544-1554.
53. Q. Peng, Y. Dong and Y. Li, *Angew. Chem. Int. Ed.*, 2003, **115**, 3135-3138.
54. X. Shen, J. Sun, G. Wang, J. Park and K. Chen, *Mater. Res. Bull.*, 2010, **45**, 766-771.
55. S. K. Meher and G. R. Rao, *J. Phys. Chem. C*, 2011, **115**, 15646-15654.
56. P.-C. Chen, G. Shen, Y. Shi, H. Chen and C. Zhou, *ACS Nano*, 2010, **4**, 4403-4411.
57. L. Li, Y. Cheah, Y. Ko, P. Teh, G. Wee, C. Wong, S. Peng and M. Srinivasan, *J. Mater. Chem. A*, 2013, **1**, 10935-10941.
58. L. Yu, L. Zhang, H. B. Wu, G. Zhang and X. W. Lou, *Energy Environ. Sci.*, 2013, **6**, 2664-2671.
59. L. Zhou, D. Zhao and X. W. Lou, *Adv. Mater.*, 2012, **24**, 745-748.
60. J. Bai, X. Li, G. Liu, Y. Qian and S. Xiong, *Adv. Funct. Mater.*, 2014, **24**, 3012-3020.
61. Y. Chen, J. Zhu, B. Qu, B. Lu and Z. Xu, *Nano Energy*, 2014, **3**, 88-94.
62. L. Li, K. H. Seng, Z. Chen, Z. Guo and H. K. Liu, *Nanoscale*, 2013, **5**, 1922-1928.

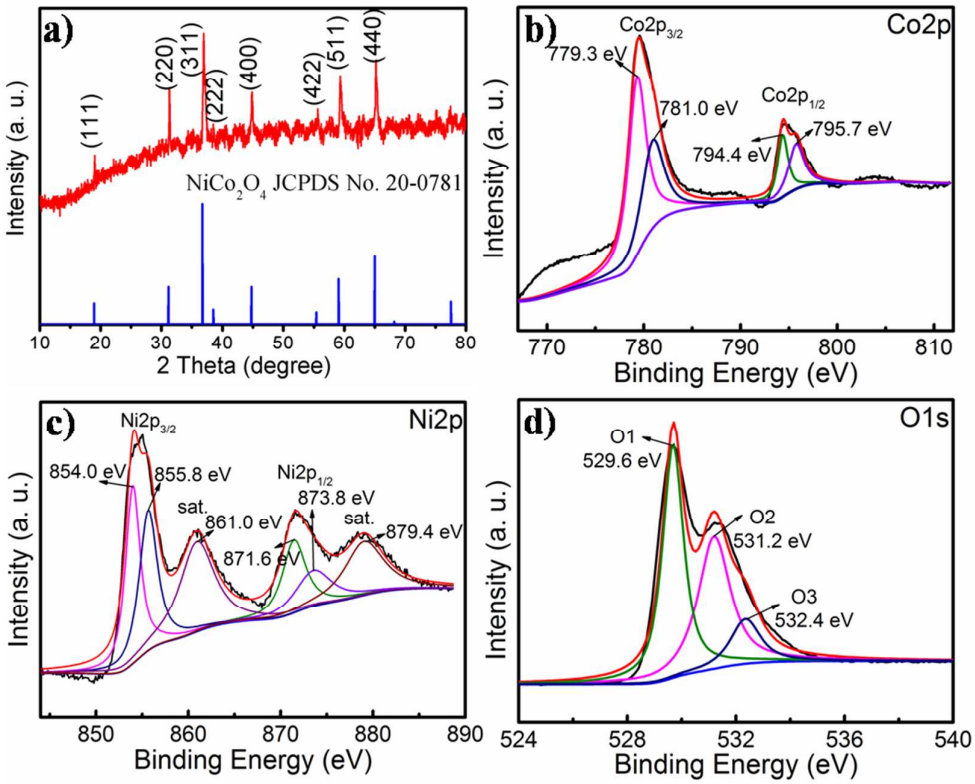

Figure 1.a) XRD pattern of NCO-M@N, b) XPS spectrum of Co2p, c) XPS spectrum of Ni2p and d) XPS spectrum of O1s for NCO-M@N.

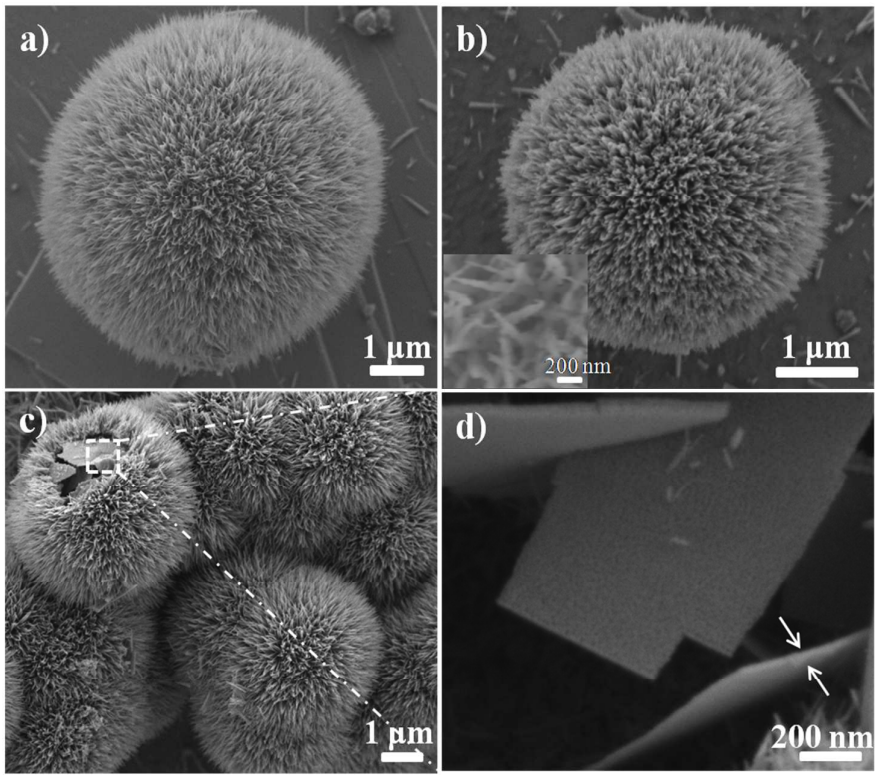

Figure 2. SEM image of a) the Co-Ni bimetallic carbonate hydroxide salts precursors, b) the dandelion-like NCO-M@N (the inset is used to describe the detail of the nanoneedles), c) the cracked NCO-M@N, d) internal nanomeshes (the local magnified image of the box in Figure 2c).

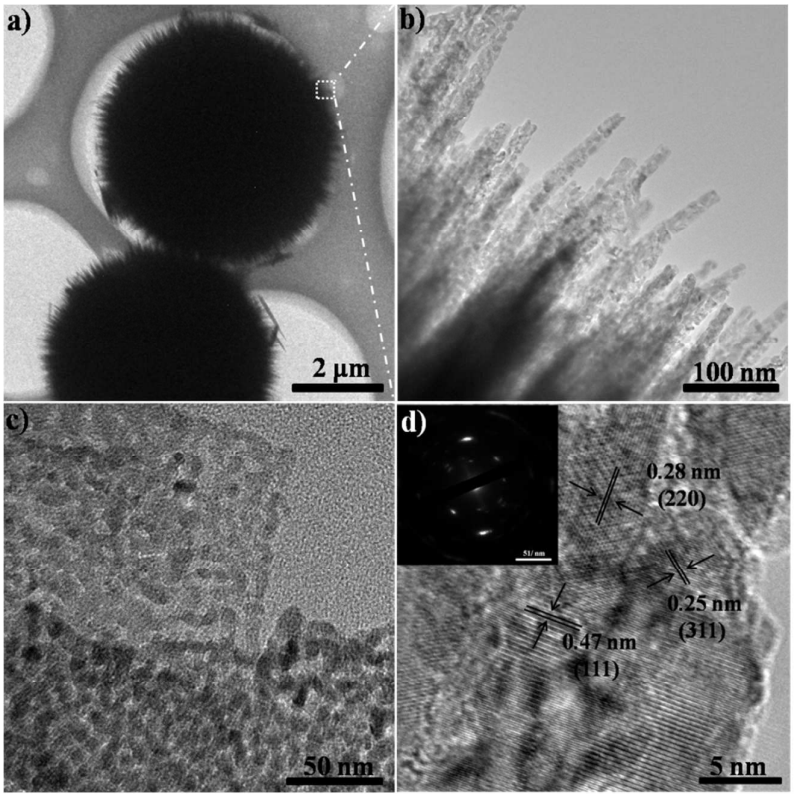

Figure 3. a) The low-magnification TEM image of NCO-M@N, b) The magnified TEM image of the external nanoneedles (the selected area of the white box in Figure 3a), c) The magnified TEM image of the internal nanomeshes, d) The HRTEM image of NCO-M@N (the inset is the SAED pattern of NCO-M@N).

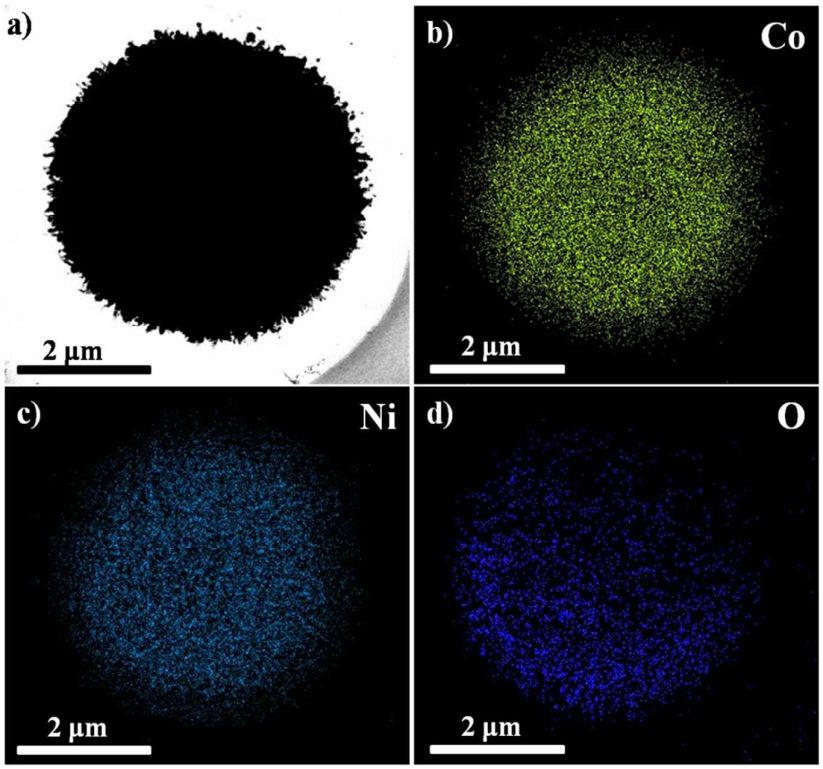

Figure 4. The dot mapping images of NCO-M@N.

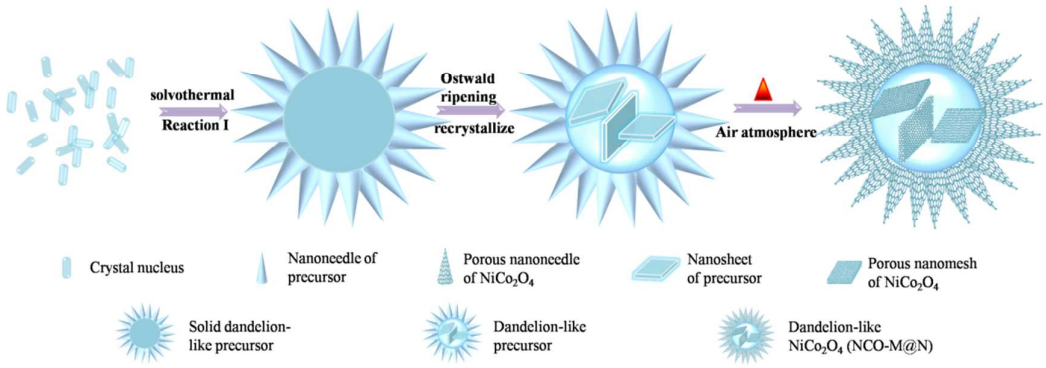

Scheme 1.Schematic illustration of the formation of the dandelion-like NCO-M@N.

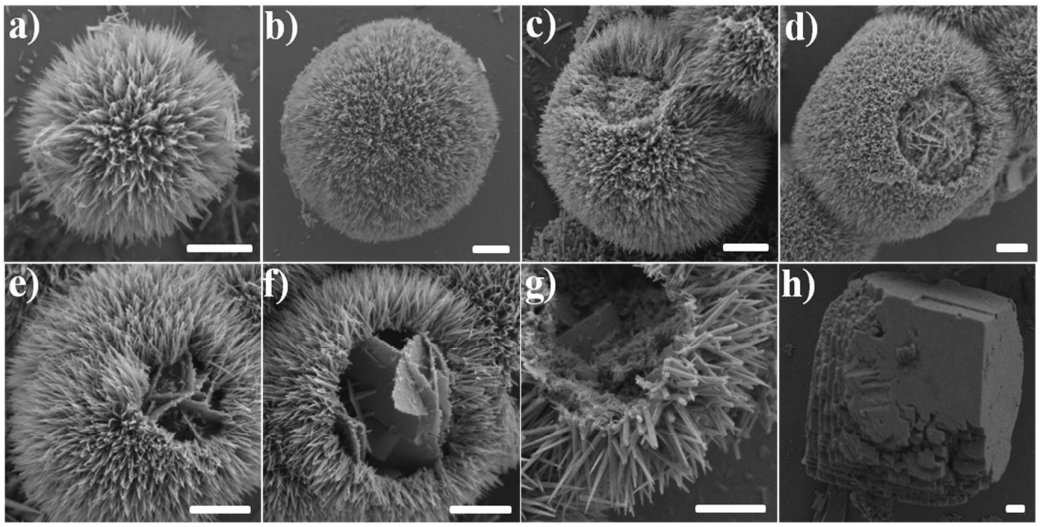

Figure 5. a)-h) SEM images of the precursor obtained after reaction for 1 h, 2 h, 4 h, 6 h, 7 h, 8 h, 9 h and 10 h, respectively. Scale bar: 1 μm.

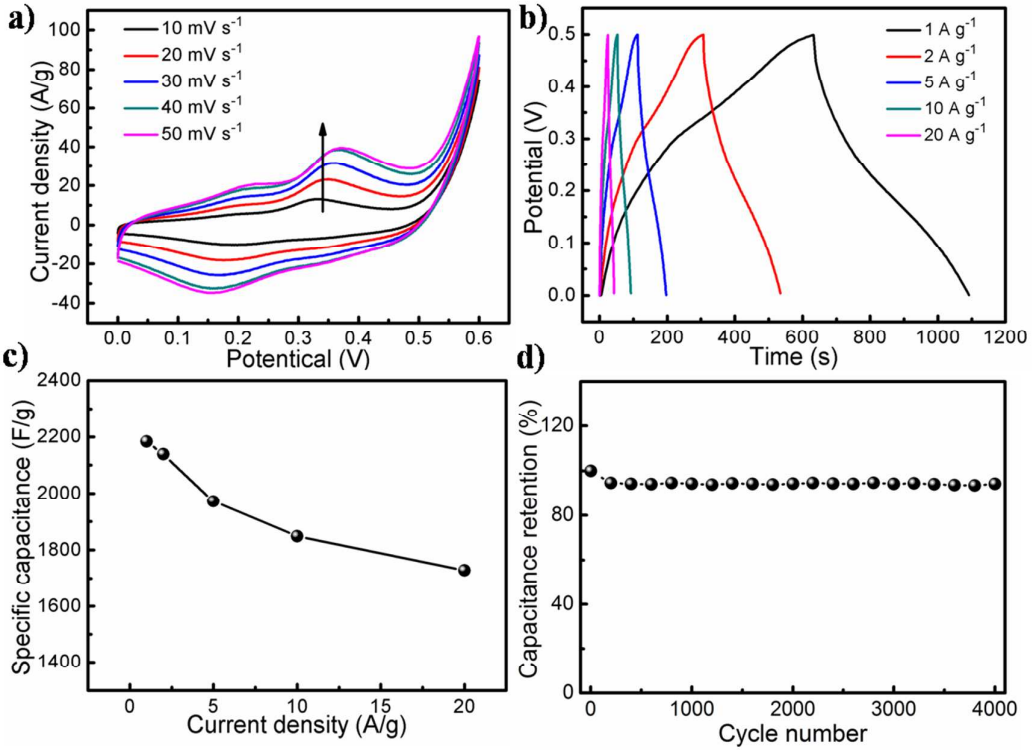

Fiugre 6. a) CV curves at various scan rates ranging from 10 to 50 mV s^{-1}, b) Charge-discharge voltage profiles at various current densities ranging from 1 to 20 A g^{-1}, c) Specific capacitance versus current densities of NCO-M@N, d) Cycling performance of the NCO-M@N electrode for 4000 cycles at a current density of 5 A g^{-1}.

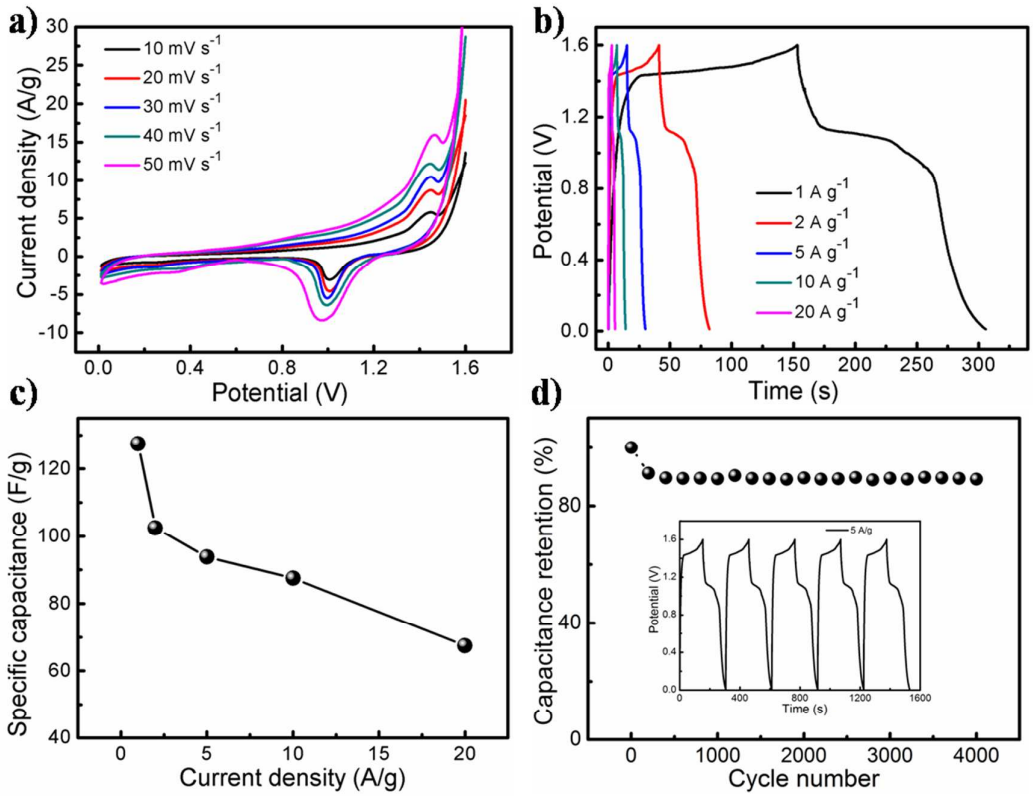

Fiugre 7. a) CV curves of the as-fabricated NCO-M@N//AC-ASC at various scan rates ranging from 10 to 50 mV s^{-1}, b) Charge-discharge voltage profiles of NCO-M@N//AC-ASC at various current densities ranging from 1 to 20 A g^{-1}, c) Specific capacitance values of the NCO-M@N//AC-ASC as function of current density, d) The cycling stability of the NCO-M@N//AC-ASC at a current density of 5 A g^{-1}(the inset is used to display the last 5 cycles of the charge-discharge curves).

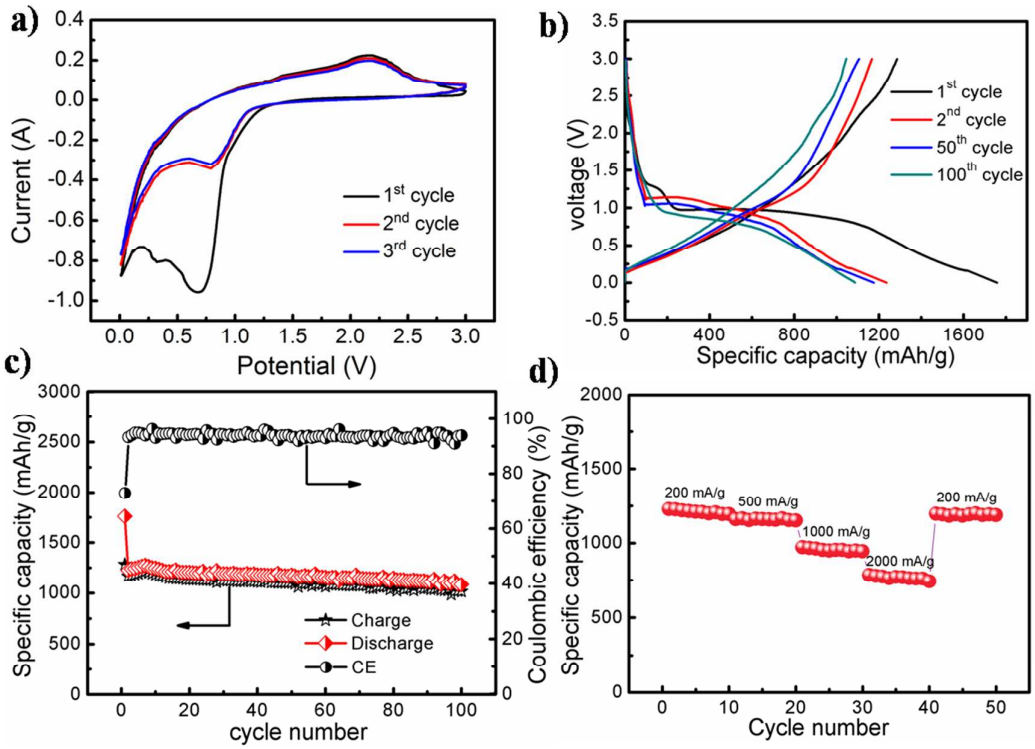

Figure 8. a) First three cyclic voltammograms (CVs) of the NCO-M@N electrode at a scan rate of 0.5 mV s^{-1} over the range of 0.01-3.0 V, b) Galvanostatic charge-discharge curves in the voltage range of 0.01-3.0 V at a charge current density of 200 mA g^{-1}, c) The charge-discharge capacities and corresponding Coulombic efficiency of the NCO-M@N electrode, d) Rate performance at different discharge rates, 200, 500, 1000 and 2000 mA g^{-1}, respectively, in the voltage range between 0.01 and 3.0 V of the NCO-M@N electrode.